

# A generalized perfect vortex beam with controllable impulse ring profile

*Junjie Yu<sup>1+</sup>, Chaofeng Miao<sup>1,2,3</sup>, Jun Wu<sup>4</sup>, and Changhe Zhou<sup>1\*</sup>*

Corresponding Authors: E-mail: [+junjiey@siom.ac.cn](mailto:junjiey@siom.ac.cn) or [\\*chazhou@mail.shcnc.ac.cn](mailto:chazhou@mail.shcnc.ac.cn)

<sup>1</sup>Lab of Information Optics and Opto-electronic Technology, Shanghai Institute of Optics and Fine Mechanics, Chinese Academy of Sciences, P. O. Box 800-211, Shanghai 201800, China

<sup>2</sup>School of Physical Science and Technology, ShanghaiTech University, Shanghai 201210, China

<sup>3</sup>University of Chinese Academy of Sciences, Beijing 100049, China

<sup>4</sup>Department of Physics, Zhejiang University of Science and Technology, Hangzhou, 310023, China

Keywords: dark perfect optical vortex; impulse ring; controllable ring profile; circular gratings; phase singularity

Perfect optical vortices (POVs) provide an enabling solution to address the predicament induced by the strong dependence of classical optical vortices on their carried topological charges. Here, a type of generalized POVs with controllable impulse ring profile was proposed and demonstrated. Especially, a type of “absolute” dark POVs surrounded by two bright ringlobes in each side was presented, which provides a perfect annular potential well along those dark impulse rings for trapping steadily low-index particles, cells, or quantum gas, etc. In further, several POVs with different impulse ring profiles, including conventional POVs with bright rings, dark POVs mentioned above, and also POVs with controllable impulse ring profile, were demonstrated. This work opens up new possibilities to reshape arbitrarily the impulse ring profile for perfect vortices, and this type of novel POVs will enrich functions of optical vortices and it should be of high interest for its potential applications in optical manipulation, both quantum and classical optical communications, enhanced optical imaging, and also novel structured pumping lasers, etc.

## 1. Introduction

An optical vortex is identified typically as a phase singularity encircled with helical wavefront, which contributes essentially to one of important fundamentals of wave phenomena. Duo to its unique properties including its carried orbital angular momentum (OAM) associated with doughnut-shaped profiles [1, 2], an optical vortex is arousing ever-increasing interest among both scientific and engineering communities. In the past decades, the optical vortex had found its exciting applications in a great variety of realms, such as STED nanoscopy [3,4], optical

manipulation [5-7], both quantum and classical OAM-multiplexing optical communications [8-10], optical vortex coronagraph [11], enhanced optical imaging [12,13], OAM-based radars [14], and recent high-intense vortex physics [15-17], etc. Nowadays, the vortex is not limited to optical wave, and it has been extended into other spectrum range, such as X-ray [18], gamma-ray [19], and THz ray [20, 21], and also other waves including twisted electric beam waves [22, 23]. However, the size of the doughnut-shaped patterns generated by conventional vortices is strongly dependent on the carried topological charge, which hampers their applications in many practical fields. In 2013, Ostrvsky and coworkers [24] introduced the concept of perfect optical vortices (POVs), which is shaped into an impulse vortex ring with its radius being quasi-independent of the topological charge. In an ideal situation, the complex amplitude of a POV could be expressed by  $\delta(r-r_0)\exp(il\varphi)$ , where  $\delta(\cdot)$  denotes the Dirac delta function,  $(r, \varphi)$  are the radial and azimuthal coordinates, and  $r_0$  is the radius of the impulse ring. Since its radial intensity profile and bright ring diameter are independent of its topological charge, this type of optical vortices offers a possibility to couple multiple OAM beams into a certain fiber with fixed annular index profile [25], and thus POVs are intriguing for their brilliant prospects in the applications for OAM multiplexing optical fiber communications. Also, this “perfect” vortex beam is of significant interest in dynamical trapping micro-particles, atoms, and quantum gases along those bright rings [26, 27]. It has demonstrated that these perfect vortices provided a possibility to transfer OAM to trapped particles along the bright impulse ring. More importantly, the steady radial intensity profile and the independent ring diameter enable one to control the rotating velocity of the trapped particles along the same orbit just by changing the topological charge. Recently, POVs are also explored for other different application purposes. Reddy *et al.* [28] demonstrated a type of non-diffracting speckles generated by scattering a POV beam through a rough surface. Zhang *et al.* [29] proposed a plasmonic structured illumination microscopy imaging technique with the use of POVs for enhancing the excitation efficiency of surface plasmon and reducing the background noise of the excited fluorescence. Also, POVs

were employed for exploration of various nonlinear phenomena, such as harmonic generation [30], parametric down-conversion [31], and perfect quantum optical vortex state [32], etc. In further, a type of vectorial perfect vortices was proposed and demonstrated, which provides more degrees of freedom in beam manipulation [33-35]. Latterly, the concept of POVs was generalized to a type of elliptic perfect optical vortices, where those symmetrical circular rings were transformed into asymmetric elliptic rings [36, 37].

However, the impulse rings of those POVs mentioned above are all bright rings, and these bright rings could also hindered their applications in some scenarios. One of important cases, for instance, is that the particles/cells will be difficultly trapped steadily along those bright rings generated by conventional POVs when their refractive index is lower than the surrounding medium. Recently, Liang *et al.* [38] proposed an interesting scheme for trapping the low-refractive-index particles with POVs, where the size of the trapped particle is comparable to the radius of the impulse rings generated by those POVs. Moreover, a point trap was needed to improve the stability of the ring trap, and that composited trap essentially can be seen as a dark ring constructed by the central point spot and the surrounding annular ring. Most recently, the same group [39] presented an attractive scheme for generation of a dark POV, coined double-ring POVs by them, through the use of the Fourier transform of azimuthal polarized Bessel beams, which can be seen essentially as the incoherent superposition of two opposite circular polarized POVs. However, the dark ring of those POVs degenerates with increase of the topological charge. Actually, in our previous paper [40], we have demonstrated that circular Dammann gratings (CDGs), which was first proposed by Zhou *et al* in 2003 [41], could provide an effective method for generation of controllable impulse rings, and predicted that this method could be used for generation of perfect vortices with controllable impulse ring profile, especially those dark POVs.

In this work, we propose a type of generalized perfect vortex beams with controllable impulse ring profiles generated by a CDG embedded with a spiral phase, whose radial intensity profile

and the diameter of the impulse ring are independent of the topological charge. Especially, one could obtain a type of “absolute” dark perfect vortex rings surrounded by two bright impulse rings in each side, by controlling the structure of the circular gratings. This work opens up new possibilities to reshape the impulse ring profile for perfect vortices, and this type of novel perfect vortices will enrich the functionalities of vortex beams and it should be of high interest for its potential applications in a range of realms, such as optical manipulations, quantum and classical optical communications, enhanced optical imaging, and also novel structured pumping lasers, etc.

## 2. Principle and Methods

### 2.1. Design Principle

It is well demonstrated that the transmission function of a circular grating could be decomposed into a series of circular sine or cosine functions with different radial frequencies, and it can be written as the sum of a Fourier series (or called Hankel series) [42],

$$T(r) = \left[ \frac{a_0}{2} + \sum_{m=1}^{\infty} a_m \cos(2\pi mr / \Lambda) \right]. \quad (1)$$

where  $(r, \theta)$  is the polar coordinate on the plane of the circular grating, and  $\Lambda$  is the radial period. After a spiral phase is embedded, the transmission function can be rewritten as,

$$\begin{aligned} T(r, \theta) &= T(r) \exp(il\theta) \\ &= \frac{a_0}{2} \exp(il\theta) + \sum_{m=1}^{\infty} a_m \cos(2\pi mr / \Lambda) \exp(il\theta). \end{aligned} \quad (2)$$

Here, the Fourier coefficient of the  $m$ th order  $a_m$  can be expressed by,

$$a_m = \int_0^{\Lambda} T(r) \cos(2\pi mr / \Lambda) dr. \quad (3)$$

The  $m$ th order of the Hankel series of the transmission function of a circular grating embedded with spiral phase depicted in Eq. (2) can also be, according to Euler’s formula, rewritten as,

$$h_m(r, \theta) = \frac{a_m \exp(il\theta)}{2} [\exp(i2\pi mr / \Lambda) + \exp(-i2\pi mr / \Lambda)]. \quad (4)$$

Noted that these two terms in the square bracket, essentially, denote an axicon pair: a negative axicon and another positive one. The coefficient  $a_m$  can be rewritten as

$$a_m = c_m + c_{-m} = |c_m| \exp(i \frac{\Delta\phi_m}{2}) + |c_{-m}| \exp(-i \frac{\Delta\phi_m}{2}), \quad (5)$$

where  $c_{\pm m} = \int_0^\Lambda T(r) \exp(\mp i2\pi mr / \Lambda) dr$ , with  $\Delta\phi_m = |\arg\{c_m\} - \arg\{c_{-m}\}|$  being the phase delay between these two coefficients and  $|c_{\pm m}|$  being their amplitudes. For binary  $(0, \pi)$  pure-phase gratings,  $|c_{+m}| = |c_{-m}|$ , and the  $m$ th order can be written further as,

$$h_m(r, \theta) = \sum_{m=1}^{\infty} |c_m| \cos(2\pi mr / \Lambda + \Delta\phi_m / 2) \exp(il\theta), \quad (6)$$

where the coefficients can be expressed as

$$c_m = \sum_{n=1}^{N-1} \int_{r_n}^{r_{n+1}} \exp([1 + (-1)^n] / 2) \exp(i2\pi mr / \Lambda) dr, \quad (7)$$

with  $\{r_n\}$  being the normalized transitional points in one period along the radial direction of the binary  $(0, \pi)$  pure-phase circular grating, which is also called circular Dammann grating, and  $N$  being the total number of the transitional points in one period. Then, the Fraunhofer diffraction field of the  $m$ th non-zeroth order can be written as,

$$H_m(\rho, \varphi) = (-i)^{l+1} \frac{k}{f} \exp(il\varphi) (u_m H_c^m + v_m H_s^m), \quad (8)$$

where,

$$H_m^c = \int_0^R \cos(2\pi mr / \Lambda) J_1(k\rho r / f) r dr, \quad (9a)$$

$$H_m^s = \int_0^R \sin(2\pi mr / \Lambda) J_1(k\rho r / f) r dr. \quad (9b)$$

The Fourier spectrum of the  $m$ th order circular cosine function embedded with a spiral phase depicted in Eq. (8) is essentially a weight sum of two impulse rings (see details in Supporting Information Note S1) with coefficients of  $u_m = \cos(\Delta\phi_m/2)$ , and  $v_m = -\sin(\Delta\phi_m/2)$ . Thus, we can control arbitrarily the impulse ring profile of the POVs by changing the phase delay  $\Delta\phi_m$  that determined by the grating structure. Given a phase delay  $\Delta\phi_m$ , one can determine the sidelobe ratio (defined as the ratio of the ringlobe to the main-ring) as

$$\beta(\Delta\phi_m) = \begin{cases} |H_m^{\min} / H_m^{\max}|^2, & \text{if } |H_m^{\max}| \geq |H_m^{\min}| \\ |H_m^{\max} / H_m^{\min}|^2, & \text{if } |H_m^{\max}| < |H_m^{\min}| \end{cases}. \quad (10)$$

According to the above equation, one can control arbitrarily the sidelobe ratio by changing the phase delay  $\Delta\phi_m$ , which is determined by the grating structure. Thus, one can control the intensity profile of the impulse rings just by changing the grating structure. For example, when the sidelobe ratio is equal to one, an “absolute” dark impulse ring surrounded by two bright rings in each side could be expected due to destructive interference. Then, the whole designing flow for generation of POVs with arbitrary impulse ring profiles can be divided into six steps as follows. Firstly, determining the period number inside the aperture and choosing the topological charge. Next, determining the sidelobe ratio of the intensity profile along the radial direction according to the application purposes. Then, calculating the phase delay  $\Delta\phi_m$  according to Eq. (10). Fourthly, searching the transitional points in each period of circular Dammann gratings by minimizing the difference of the target phase  $\Delta\phi_m = \arctan(W_m)/2$  and the phase delay between the axicon pair at  $m$ th order. Fifthly, by using the transitional points as the initial solution, optimizing the transitional points by minimizing the difference of the target sidelobe ratio and maximizing the feature size for certain period number. Finally, after transitional points being determined, one can obtain the grating structure by arranging the coaxial rings periodically along the radial direction with the designed period number.

It should be noted that, the integrals in Eqs. (9a) and (9b) will approach to the  $l$ th order Hankel transform of circular cosine and sine functions depicted in Eqs. (s6a) and (s6b) (see Supporting Information Note S1), when the aperture size  $R$  is large enough. However, in practice, it is impossible to obtain an aperture with infinite large size, and the limited aperture determines that the period number inside the aperture is also limited. When the period number is not large enough, the phase delay is sensitive to the period number and thus we need to reoptimize the grating structure when the period number is different.

## 2.2 Experimental Scheme

In order to verify the designed gratings embedded with vortices for generation of generalized POVs, we design a proof-of-principle experiment setup for investigation of those generalized POVs as shown in Fig 1. An expanded and collimated laser beam operating at 532 nm (Coherent Verdi 6) is used as the light source. The laser beam is passing through a polarizer and then it is divided into two parts by a polarized beam splitter cube PBS1. The transmitted part is horizontal polarized ( $p$ -polarization) and it is directed by a nonpolarized beam splitter cube BS1 onto the liquid crystal display (LCD) of a programmable spatial light modulator (SLM, HoloEye, Pluto NIR-011, pixel size 8  $\mu\text{m}$ , and 1080 $\times$ 1920 pixels), where the phase of circular Dammann gratings embedded with a spiral phase encoding into a blazed grating is loaded. The purpose of the blazed grating is for removing the unmodulated zeroth order diffracted from the SLM. Next, the modulated beam is reflected back from the LCD and then it is relayed by a confocal lens pair L3 and L4 with a tunable iris for singling out the first diffraction order, carrying the phase of gratings embedded with spiral phase. The filtered field is then focused by a convergent lens L5 with focal length of 600 mm, and a COMS camera (Edmund Optics, EO2323M, pixel size 4.8  $\mu\text{m}$ , and 1200 $\times$ 1920 pixels) is located in the back focal plane of the lens L5 for detecting the field. Another part is vertical polarized ( $s$ -polarization) and it is reflected by a reflective mirror M. Then, this reference part is finally combined with the first part by another polarized beam splitter cube PBS2 and the interference field pass a  $\lambda/4$  waveplate and a polarizer P2, and

then it is detected by the CMOS camera. Care must be taken to carefully adjust the distance between the L1 and L2 to make sure the expanded beam is free of spherical aberration. A home-made shearing interferometer is used here for examining the transmitted wavefront. Besides the interference fields, the focused field of the generated POVs on the focal plane is also captured by the CMOS camera when the reference beam is blocked.

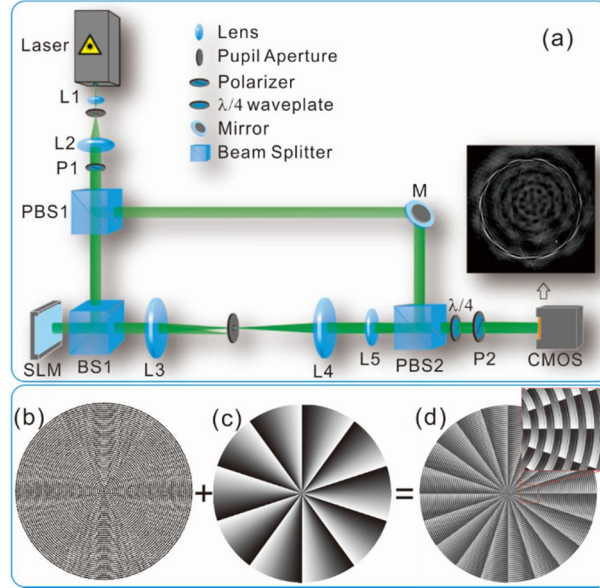


**Figure 1.** Schematic diagrams for the experimental scheme. (a) Proof-of-principle experimental setup. L1~2 are lenses for expanding and collimation. L3 and L4 are a confocal lens pair, and L5 is the focusing lens; PBS1~2 are polarized beam splitter cubes; BS1 is a nonpolarized beam splitter; M is a reflective mirror; SLM denotes a spatial light modulator; P1~2 denote polarizers;  $\lambda/4$  denotes a quarter waveplate. CMOS denotes a Complementary Metal-Oxide Semiconductor camera; (b) a typical phase structure of a typical binary Circular Dammann grating; (c) a typical phase distribution of a spiral phase with charge of  $l=10$ ; (d) the phase distribution of the CDG embedded with vortex phase for generation of perfect optical vortex with tunable impulse profile. The inset shows the enlarge part in the rectangular area.

### 3. Results and Discussion

#### 3.1 Dark perfect optical vortices

As pointed out above, one can control arbitrarily the impulse ring profile by changing the phase delay between those two impulse rings (through changing the grating structure). One important case is that a dark ring surrounded by two bright ringlobes in each size could be realized when destructive interference is achieved for those inwards- and outwards-oriented impulse rings.

Here, as examples, we design four type of circular gratings embedded with spiral phase for generation of dark perfect vortices with topological charges of  $l = 1, -5, 15, 20$ , respectively, and the period number inside the aperture is set as 20. The normalized transitional points  $\{r_n\}$  in the first half-period along the radial direction of these CDGs are  $\{0.36309, 0.48272\}$ ,  $\{0.44996, 0.26388\}$ ,  $\{0.47858, 0.28769\}$ , and  $\{0.03218, 0.21814\}$  for those four dark POVs, respectively. The phase distribution in the last half-period is inversed and thus those transitional points can be derived by  $\{r_n + 0.5\}$  [43]. Figure 3 illustrates the experimental results of those four POVs with dark rings, compared with their simulation results. It is seen clearly that dark perfect optical vortices are well generated as expected. Moreover, one can also see from those intensity profiles along those dotted line crossing the center that the valley of those dark rings are always kept low enough for all cases, which suggest that the sharpness of those dark POVs are almost independent of the topological charge. In further, the interference fringes of those POVs with the plane wave are also shown. It is seen that those interferograms are distinguished by those petal-like patterns and the whole interferograms possess the  $l$ -fold rotational symmetry. Further, the amplitude of the topological charge can be figured out as  $l$  if the number of those petals is  $2l$ . It is indicated that the amplitude of topological charges carried by those dark POVs are 1, 5, 15, 20, which is in a good agreement with theoretical expectations. Noted that the interference fringes on the focal plane are  $l$ -fold rotational symmetric and one could not easily identify the sign of the topological charge from these interferograms on the focal plane. Also, it is noticed that the symmetry of the experimental interferograms is not perfect, which is mainly caused by residual aberrations and also alignment errors. However, the sign can be identified by checking the rotating direction of interference fringes on defocused planes. The petal-like patterns will become a series of helixes on the defocused plane, and the sign of the topological charge can be identified by the rotating direction of those helixes. Figure 4 shows the simulational and experimental results of the intensity distribution and interference fringes on a defocused plane for two dark POVs with topological charge of  $l = 10$  (a) and  $l = -5$  (b). It is

shown clearly that the helix-like fringes are obtained as prediction, and the sign of the topological charge can be identified by the chirality of helices. For those interferograms on the defocused plane before the focus, the clockwise helices indicate a positive charge while the anticlockwise helices suggest a negative one, and the rotational direction of those helices are inverted for those interferograms on the defocused planes after the focus.

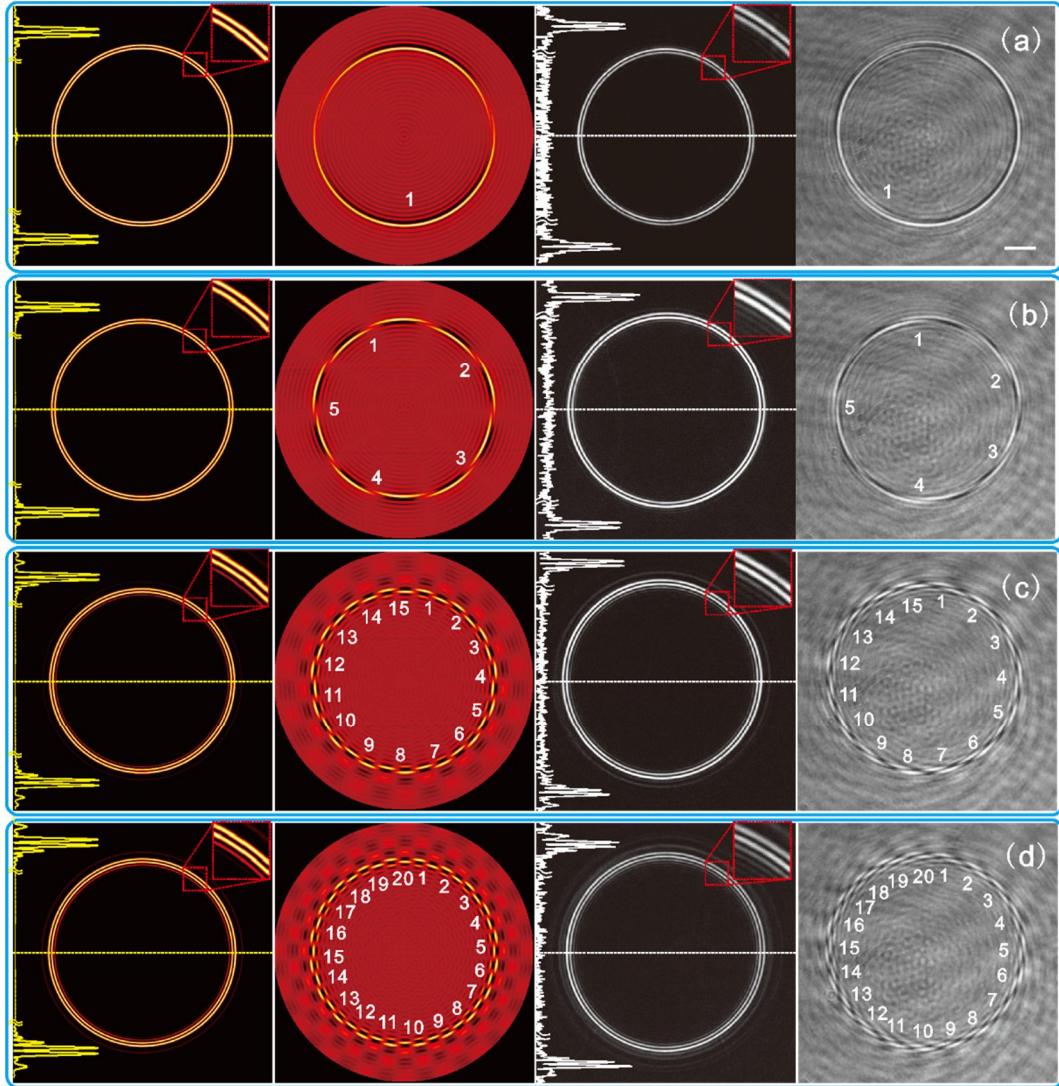


**Figure 2.** Simulation and experimental results for dark perfect optical vortices generated by CDGs with period number of 20 inside the aperture of the focusing lens. (a) dark perfect optical vortex with topological charge of  $l=1$ ; (b) dark perfect optical vortex with topological charge of  $l=10$ ; (c) dark perfect optical vortex with topological charge of  $l=20$ . In each box, the simulation result of the intensity distribution is in the top-left corner, and the simulation result of the interference is in the top-right corner; the experimental result of the intensity distribution is in the bottom-left corner and the interference result is in the bottom-right corner. The insets are enlarged part for the dark impulse rings in the rectangular area. The scale bar denotes  $300 \mu\text{m}$ .

In order to verify the generated vortices further, the phase of the generated dark POVs with topological charge of  $l=10$  and  $l=-5$  on the defocused planes (defocus distance is about  $\Delta d=25$  mm) are extracted by six-step phase-shifted interferograms. By rotating the axis of the polarizer P2 at six different angles with a step of  $\pi/6$  rad, one can extract the phase on the defocused plane using those six phase-shifted interferograms. From this figure, it is seen clearly that the amplitude of the topological charge of the spiral phase are  $|l| = 10$  and  $|l| = 5$  are for those two dark-ring POVs, respectively. Furthermore, one can also see that the anticlockwise phase gradient direction indicates a positive topological charge ( $l = 10$ ), while the clockwise one suggests a negative topological charge ( $l = -5$ ). It should be noted that the gradient of the extracted phase is not very good, which is mainly caused by mechanical vibrations, air disturbances, temperature fluctuations, and also instability of the laser source.

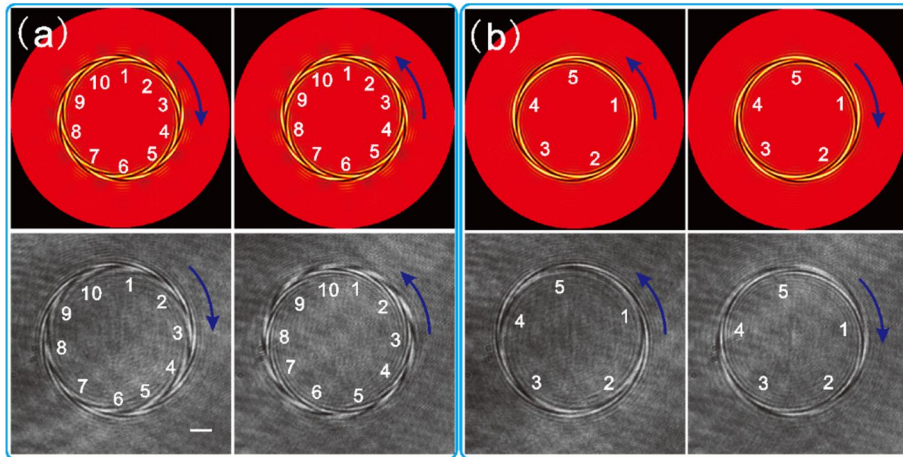


**Figure 3.** Simulation and experimental results of the interferograms on the defocused planes for dark perfect optical vortices (with defocus distance  $\Delta d=10$  mm). (a) dark perfect optical vortex with topological charge of  $l=10$ ; (b) dark perfect optical vortex with topological charge of  $l=-5$ ; In each box, the simulation results are shown in the first row and the experiment results are shown in the second row. The results in the first column are the interference fringes before the focal plane and the results in the second column are the interference fringes after the focal plane. The scale bar denotes  $300 \mu\text{m}$ .

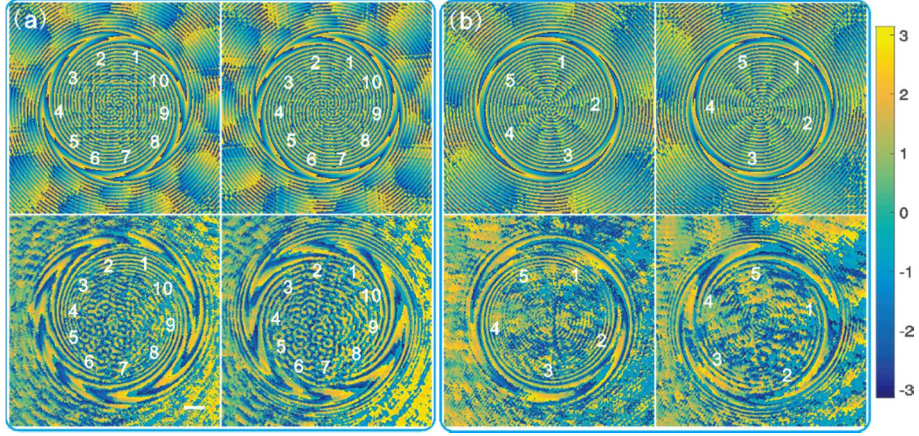


**Figure 4.** Simulation and experimental results of the phase distribution on the defocused plane (with defocus distance  $\Delta d=25$  mm) for dark perfect optical vortices with topological charge of  $l=10$  (a) and  $l=5$  (b). In each box, the simulation results are shown in the first row and the experiment results are shown in the second row. The results in the first column are phase distribution on the defocused plane before the focus and the results in the second column are the phase distribution on the defocused plane after the focus. The scale bar denotes  $300 \mu\text{m}$ .

Therefore, the type of dark perfect optical vortices surrounded by two bright ringlobes in each side proposed here is an “absolute” dark ring due to destructive interference, which provides an annular potential well along those dark impulse rings. This annular potential well could be used for trapping steadily low-index particles, cell, or quantum gas, etc., and the orbital angular momentum carried by those dark POVs to trapped targets. Different from the method proposed by Liang *et al* [38], this scheme proposed here is essentially the coherent superposition of two impulse rings, one inside-oriented and another outside-oriented ones. Thus, one can control the impulse ring profile by changing the phase delay between those two impulse rings. As demonstrated by Liang *et al*, there is residual non-zero intensity in the dark ring generated by using their scheme. Moreover, the residual non-zero valley is higher for larger topological charge, which indicates that the sharpness of the potential well will degenerate for those POVs with large topological charge. The dark POVs proposed here could totally overcome this drawback.

### 3.2. Bright perfect optical vortices

Besides the dark POVs, one can also obtain the bright POVs by choosing the phase delay

resulting in constructive interference. In this case, the sidelobe ratio reaches its minimum value by optimizing the structures of CDGs. Figure 5 illustrates the results of four bright POVs with topological charge of  $l=1, -5, 15,$  and  $20$  generated by CDGs with period number of  $20$  inside the aperture of the focusing lens. The normalized transitional points  $\{r_n\}$  in the first half-period of CDGs are  $\{0.14655, 0.46455\}$ ,  $\{0.07592, 0.48340\}$ ,  $\{0.02971, 0.12886\}$ , and  $\{0.029716, 0.48696\}$  for those four bright POVs aforementioned, respectively. It is seen that a bright impulse ring accompanied by two weak equal-intensity ringlobes are well generated as prediction, with consideration of various errors, such as alignment errors, phase errors induced by imperfect gamma correction of the SLM, and also various residual aberrations of the focusing system. In this case, the number of the bright petals of the interference field on the focal plane indicate the amplitude of the topological charge, and the sign can be identified by checking the rotational direction of the helices of the interferograms on the defocused planes, similar to dark POVs aforementioned. It should be noted that the sidelobe ratio increases with the topological charge, which will discuss further in the following.

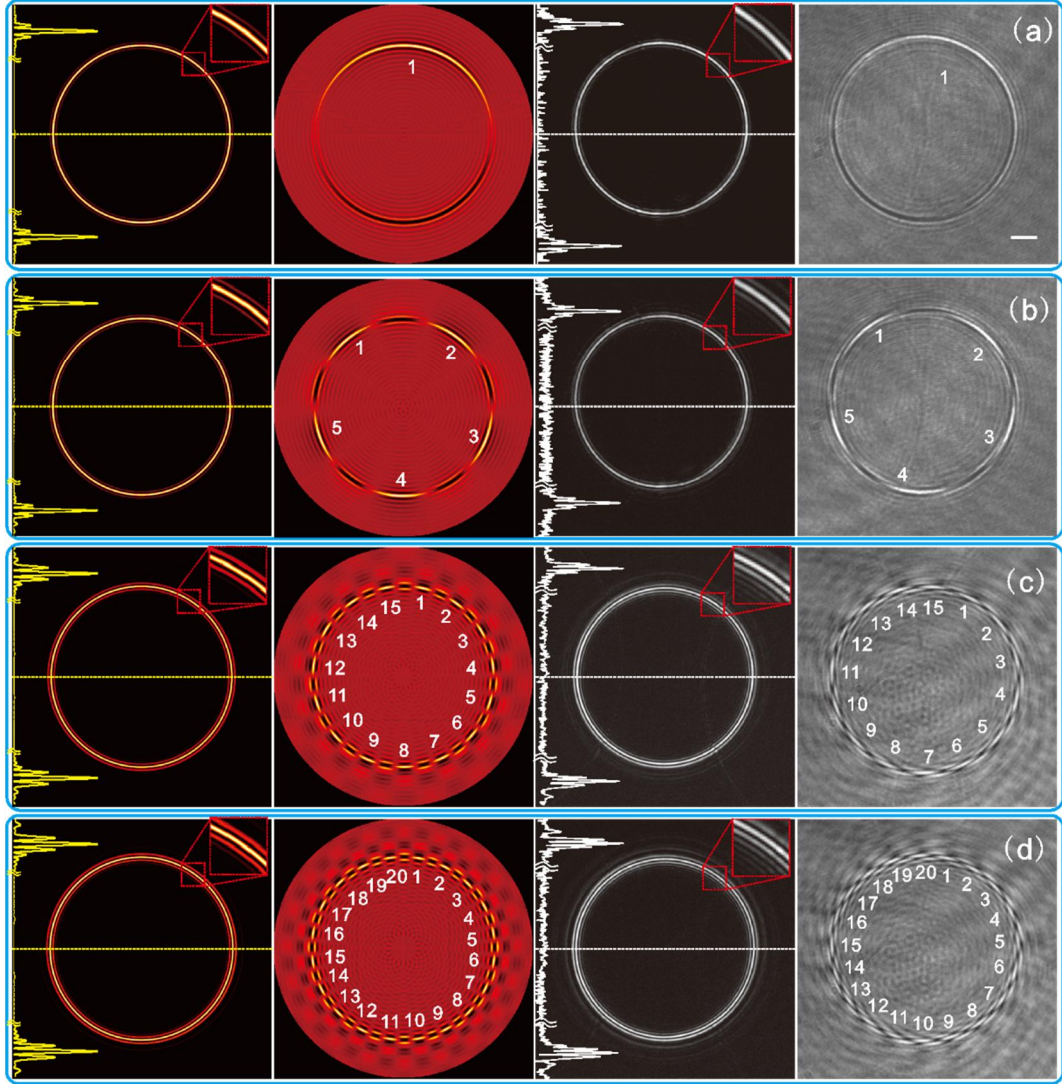


**Figure 5.** Simulation and experimental results for bright perfect optical vortices generated by CDGs with period number of 20 inside the aperture of the focusing lens. (a) bright POV with topological charge of  $l=1$ ; (b) bright POV with topological charge of  $l=10$ ; (c) bright POV with topological charge of  $l=20$ . In each box, the simulation result of the intensity distribution is in the top-left corner, and the simulation result of the interference is in the top-right corner; the experimental result of the intensity distribution is in the bottom-left corner and the interference result is in the bottom-right corner. The insets are enlarged part for the dark impulse rings in the rectangular area. The scale bar denotes  $300 \mu\text{m}$ .

### 3.3. Perfect optical vortices with arbitrary impulse ring profile

It has been shown that, one can control the impulse ring profile arbitrarily by changing the weight coefficient, since the Fourier spectrum of each diffraction order is essentially a weight sum of two impulse rings. In this part, we will demonstrate that the impulse ring profile can be arbitrarily adjusted by changing the grating structure of CDGs. As examples, we design a POV with topological charge of  $l=10$  with six different impulse ring profile, with a whole cycle

transition gradually from a dark ring to a bright ring. Figure 6 shows the curve of the sidelobe ratio versus the phase delay under the condition of charge  $l=10$  and period number inside aperture of  $N=30$ . From this figure, one can see clearly how the sidelobe ratio is influenced when the phase delay  $\Delta\phi_m$  is gradually varied in the range of  $[0, 2\pi]$ . It can be seen that, when  $\Delta\phi_m=0$ , the sidelobe ratio is 0.41 and a single bright impulse ring accompanied by a ringlobe outside is generated. When  $\Delta\phi_m$  continues to increase, the sidelobe ratio starts to decrease and then it reaches its minimum value of 0.28 at  $\Delta\phi_m=0.2122\pi$ . In this case, the Hankel spectrum is the result of constructive interference of those inwards- and outwards-oriented impulse rings and thus a bright ring is obtained at the  $m$ th order. Actually, this case is the best solution of POVs for side-lobe suppression. Then, when  $\Delta\phi_m$  increases further, the sidelobe ratio starts to increase gradually to its maximum value at the point of  $\Delta\phi_m=1.3499\pi$ . This time, the spectrum is the result of destructive interference of those inwards- and outwards-oriented impulse rings and thus a dark ring surrounded by two bright ringlobes is generated. When  $\Delta\phi_m$  continues to increase until it reaches  $2\pi$ , the sidelobe ratio decrease again and at last it reaches its initial value again. Till now, a full cycle of the evaluation of the impulse ring of the spectrum of the  $m$ th order circular cosine function is discussed when the phase delay is  $\Delta\phi_m$  is gradually varied. Here, as examples, six different POVs (with topological charge of  $l=10$ ) with different impulse ring profiles are also shown in Fig. 6. It is shown that an impulse ring with 1/3 lobing outside, 1/3 lobing inside, 2/3 lobing inside, 2/3 lobing outside and also a bright and a dark POV, could be obtained when phase delay are  $\Delta\phi_m=0.1204\pi, 0.3733\pi, 1.0095\pi, 1.663\pi, 0.2122\pi$ , and  $1.3499\pi$ , respectively. After further optimization, the normalized transitional points  $\{r_n\}$  in the first half-period for those CDGs are  $\{0.03723, 0.2309\}$ ,  $\{0.06364, 0.20280\}$ ,  $\{0.04368, 0.45274\}$ ,  $\{0.32144, 0.47779\}$ ,  $\{0.01662, 0.20280\}$ ,  $\{0.38419, 0.46847\}$  for those six POVs with different impulse ring profiles, respectively. It is seen explicitly that one could control the impulse ring profile of the POVs by changing the phase delay, which is finally determined by

the grating structure of CDGs, and an impulse ring with 1/3 lobing outside, 1/3 lobing inside, 2/3 lobing inside, 2/3 lobing outside and also a bright and a dark POV are well generated as prediction. The interferograms on the focal planes indicate that those POVs carrying embedded spiral phase with topological charge of  $l=10$ . A much more subtle transition from a bright POV to a dark one and then again to a bright POV is demonstrated in Supplementary Media. Thus, the method proposed here opens an avenue to reshaping arbitrarily the impulse ring profile of POVs by changing the grating structure of a CDG.

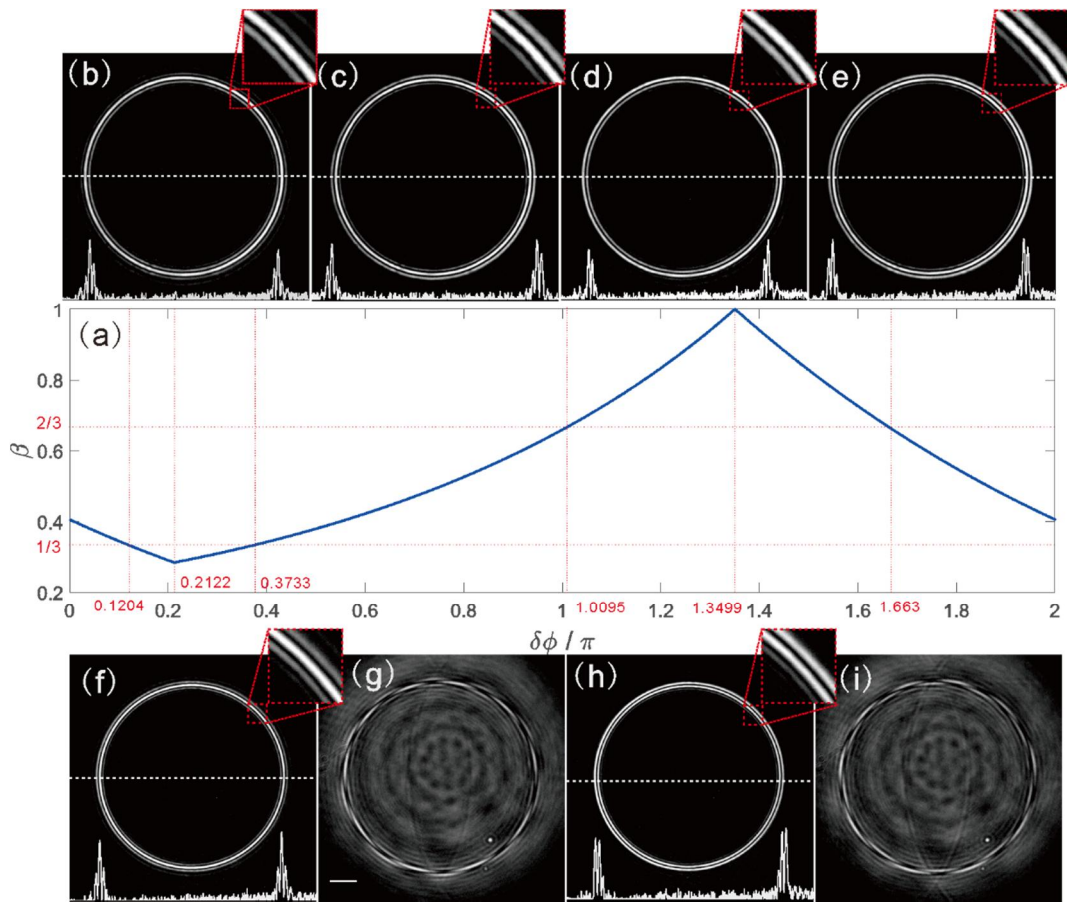


**Figure 6.** Simulation and experimental results for perfect optical vortices with topological charge of  $l=10$  with arbitrary impulse ring profile generated by CDGs with period number of  $N=30$  inside the aperture of the focusing lens. (a) The curve of the sidelobe ratio  $b$  as the function of the phase difference  $\delta\phi$ ; (b) the perfect optical vortex with sidelobe ratio of 1/3 with the ringlobe outside; (c) the perfect optical vortex with sidelobe ratio of 1/3 with the lobing inside; (d) the perfect optical vortex with sidelobe ratio of 2/3 with the lobing inside; (e) the perfect optical vortex with sidelobe ratio of 2/3 with the lobing outside; (f) the perfect optical vortex with bright impulse ring profile (with smallest sidelobe ratio), and (g) denotes its interferogram on the focal plane; (h) the perfect optical vortex with dark impulse ring profile (with unity sidelobe ratio), and (i) is its interferogram on the focal plane. The scale bar denotes 500  $\mu\text{m}$ .

### 3.4 Characterization of Perfect optical vortices

Up to now, we have demonstrated that a generalized perfect optical vortex with controllable impulse ring profile could be well generated as expectation. Here, we will discuss in this section how the performance parameters of the POVs generated by CDGs embedded with spiral phase are influenced by the topological charge and period number, which include the ring size, ring width and also sidelobe ratio. Figure 7 shows the experimental and also simulation results of the influence. It can be seen from Fig. 7a that the ring size increases with the topological charge both for bright and dark POVs and the increment is much smaller than its ring radius. So, similar to those all “perfect” optical vortices reported in the past [24, 25, 44, 45], the POVs proposed here are also only quasi-perfect in the strict sense. The influence of topological charge on the ring width is shown in Fig. 7b, from which one can see that the ring width decreases slightly with the topological charge for bright POVs, while those ring width for dark POVs are nearly invariable. Further, the ring width of the dark POVs is smaller than that of bright POVs. Figure 7c shows the sidelobe ratios versus the topological charge. It is seen that the sidelobe ratios are all nearly unity for those dark POVs, which indicates the dark POVs are in high quality. However, those sidelobe ratios increase with the charge for those bright POVs. Figure 7d-f show the ring radii, ring width, and sidelobe ratio versus the period number inside the focusing aperture. It is shown that the ring radius is linearly increased with the period number both for bright and dark POVs. One can also see from Fig. 7e that the ring width are nearly constant with the increase of the period number. It should be noted that the sidelobe ratio for those bright POVs decrease with the period number, while that of dark POVs are nearly invariable. It suggests that one can effectively reduce the sidelobe by increasing the period number inside the focusing lens.

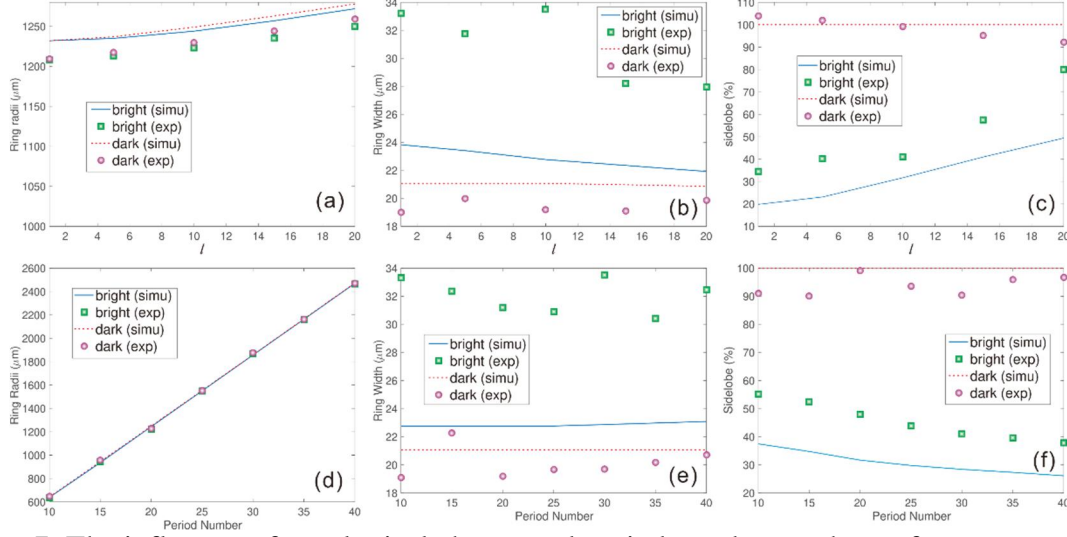


**Figure 7.** The influence of topological charge and period number on the performance parameter of perfect optical vortices with bright and dark impulse ring profile generated by CDGs. (a) the ring radius as the function of the topological charge; (b) the ring width as the function of topological charge; (c) the sidelobe ratio as the function of topological charge; (d) the ring radius versus the period number inside the focusing aperture; (e) the ring width versus the period number inside the focusing aperture; (f) the sidelobe ratio versus the period number inside the focusing aperture. In each subfigure, the blue solid line denotes the simulation result of POVs with bright impulse ring profile (bright POVs), and red broken line denotes the simulation result of POVs with dark impulse ring profile (dark POVs); the square denotes the experimental result of bright POVs and the circle is the experimental result of dark POVs.

#### 4. Conclusion and outlook

Perfect optical vortices enable one overcome the shortcut induced by the strong dependence of ring diameter to the topological charge for those conventional optical vortices. However, perfect optical vortices are all bright impulse rings in the past. A type of more generalized POVs, especially a type of “absolute” dark POVs, is proposed. As examples, several dark POVs are demonstrated and the experimental results agree well with the theoretical predictions. The interference field can be used for detecting the topological charges. Also, this method can be used for generation of conventional bright POVs, and several examples are demonstrated both theoretically and experimentally. It is shown that a bright impulse rings can be well generated compared with other schemes aforementioned. In further, a POV with controllable impulse-ring profile were demonstrated. This type of more generalized perfect optical vortices opens up new possibilities to reshape the impulse ring profile for perfect vortices, and this type of novel perfect vortices will enrich the attractive subject of singularity optics and it should be of high

interest for its potential applications in a variety of areas, such as optical manipulations, optical communications, enhanced optical imaging, and also novel structured pumping lasers, etc. Recently, micro-/nano-cavity lasers, especially micro-/nano-ring lasers, are attracting considerable interest for their high quantum yields, tunable emission wavelength, and easy integration [46]. The impulse ring proposed here could be an optimal option for pumping those micro-/nano-ring lasers.

## References

- [1] L. Allen, M. W. Beijersbergen, R. J. C. Spreeuw, and J. P. Woerdman, “Orbital angular momentum of light and the transformation of Laguerre-Gaussian laser modes”, *Phys. Rev. A* **45**, 8185-8189 (1992).
- [2] A. M. Yao and M. J. Padgett, “Orbital angular momentum: origins, behavior and applications”, *Adv. Opt. Photon.* **3(2)**, 161-204 (2011).
- [3] S. W. Hell and J. Wichmann, “Breaking the diffraction resolution limit by stimulated emission: stimulated-emission-depletion fluorescence microscopy”, *Opt. Lett.* **19(11)**, 780-782 (1994).
- [4] M Kamper, H. Ta, N. A. Jensen, S. W. Hell, and S. Jakobs, “Near-infrared STED nanoscopy with an engineered bacterial phytochrome”, *Nature Commun.* **9**, 4762 (2018).
- [5] Y. Roichman, B. Sun, Y. Roichman, J. Amato-Grill, and D. G. Grier, “Optical forces arising from phase gradients”, *Phys. Rev. Lett.* **100**, 013602 (2008).
- [6] M. Woerdemann, C. Alpmann, M. Esseling, and C. Denz, “Advanced optical trapping by complex beam shaping”, *Laser & Photon. Rev.* **7**, 839-854 (2013).
- [7] G. Chen, X. Huang, C. Xu, L. Huang, J. Xie, and D. Deng, “Propagation properties of autofocusing off-axis hollow vortex Gaussian beams in free space”, *Opt. Express* **27(5)**, 6357 (2019).
- [8] G. Molina-Terriza, A. Vaziri, J. Řeháček, Z. Hradil, and A. Zeilinger, “Triggered Qutrits for Quantum Communication Protocols”, *Phys. Rev. Lett.* **92**, 167903 (2004).
- [9] N. Bozinovic, Y. Yue, Y. Ren, M. Tur, P. Kristensen, H. Huang, A. E. Willner, and S. Ramachandran, “Terabit-scale orbital angular momentum mode division multiplexing in fibers”, *Science* **340**, 1545-1548 (2013).
- [10] A. E. Willner, “Vector-mode multiplexing brings an additional approach for capacity growth in optical fibers”, *Light: Sci. & Appl.* **7**, 18002 (2018).
- [11] G. Foo, D. M. Palacios, and G. A. Swartzlander, “Optical vortex coronagraph”, *Opt. Lett.*, **30**, 3308-3310 (2005).
- [12] S. Fürhapter, A. Jesacher, S. Bernet, and M. Ritsch-Marte, “Spiral phase contrast imaging in microscopy”, *Opt. Express*, **13(3)**, 689-694 (2005).
- [13] Y. Pan, W. Jia, J. Yu, K. Dobson, C. Zhou, Y. Wang, and T.-C. Poon, “Edge extraction using a time-varying vortex beam in incoherent digital holography”, *Opt. Lett.*, **39(14)**, 4176-4179 (2014).
- [14] T. Yuan, Y. Cheng, H. Wang, Y. Qin, and B. Fan, “Radar imaging using electromagnetic wave carrying orbital angular momentum”, *J. Electron. Imaging*, **26**, 023016 (2017).

- [15] M. Zuerch, C. Kern, P. Hansinger, A. Dreischuh, and C. Spielmann, “Strong-field physics with singular light beams”, *Nature Phys.*, **8**, 743-746 (2012).
- [16] A. Denoëud, L. Chopineau, A. Leblanc, and F. Quere, “Interaction of ultraintense laser vortices with plasma mirrors”, *Phys. Rev. Lett.*, **118**, 033902 (2017).
- [17] W. Wang, C. Jiang, B. Shen, F. Yuan, Z. Gan, H. Zhang, S. H. Zhai, and Z. Xu, “New optical manipulation of relativistic vortex cutter”, *Phys. Rev. Lett.*, **122**, 024801 (2019).
- [18] S. Sasaki and I. McNulty, “Proposal for generating brilliant x-ray beams carrying orbital angular momentum”, *Phys. Rev. Lett.*, **100**, 124801 (2008).
- [19] Y. Chen, J. Li, K. Z. Hatsagortsyan, and C. H. Keitel, “ $\gamma$ -Ray Beams with Large Orbital Angular Momentum via Nonlinear Compton Scattering with Radiation Reaction”, *Phys. Rev. Lett.* **121**, 074801 (2018).
- [20] R. Imai, N. Kanda, T. Higuchi, K. Konishi, and M. Kuwata-Gonokami, “Generation of broadband terahertz vortex beams”, *Opt. Lett.*, **39**, 3714-3717 (2014).
- [21] A. A. Sirenko, P. Marsik, C. Bernhard, T. N. Stanislavchuk, V. Kiryukhin, and S.-W. Cheong, “Terahertz vortex beam as a spectroscopic probe of magnetic excitations”, *Phys. Rev. Lett.* **122**, 237401 (2019).
- [22] M. Uchida and A. Tonomura, “Generation of electron beams carrying orbital angular momentum”, *Nature* **464**, 737-739 (2010).
- [23] A. J. Silenko, P. Zhang, and L. Zou, “Manipulating twisted electron beams”, *Phys. Rev. Lett.* **119**, 243903 (2017).
- [24] A. S. Ostrovsky, C. Rickenstorff-Parrao, and V. Arrizón, “Generation of the “perfect” optical vortex using a liquid-crystal spatial light modulator”, *Opt. Lett.* **38(4)**, 534-536 (2013).
- [25] C. Brunet, P. Vaity, Y. Messaddeq, S. LaRochelle, and L. A. Rusch, “Design, fabrication and validation of an OAM fiber supporting 36 states”, *Opt. Express* **22(21)**, 26117-26127 (2014).
- [26] M. Chen, M. Mazilu, Y. Arita, E. M. Wright, and K. Dholakia, “Dynamics of microparticles trapped in a perfect vortex beam”, *Opt. Lett.* **38(22)**, 4919-4922 (2013).
- [27] R. Paez-Lopez, U. Ruiz, V. Arrizon, and R. Ramos-Garcia, “Optical manipulation using optimal annular vortices”, *Opt. Lett.* **41(17)**, 4138-4141 (2016).
- [28] S. G. Reddy, P. Chithrabhanu, P. Vaity, A. Aadhi, S. Prabhakar, and R. P. Singh, “Non-diffracting speckles of a perfect vortex beam”, *J. Opt.* **18**, 055602 (2016).

- [29] C. Zhang, C. Min, L. Du, and X. C. Yuan, “Perfect optical vortex enhanced surface plasmon excitation for plasmonic structured illumination microscopy imaging”, *Appl. Phys. Lett.* **108**, 201601 (2016).
- [30] P. Li, Y. Zhang, S. Liu, C. Ma, L. Han, H. Cheng, and J. Zhao, “Generation of perfect vectorial vortex beams”, *Opt. Lett.* **41(10)**, 2205-2208 (2016).
- [31] S. Fu, C. Gao, T. Wang, S. Zhang, and Y. Zhai, “Simultaneous generation of multiple perfect polarization vortices with selective spatial states in various diffraction orders”, *Opt. Lett.* **41**, 5454-5457 (2016).
- [32] Y. Liu, Y. Ke, J. Zhou, Y. Liu, H. Luo, S. Wen, and D. Fan, “Generation of perfect vortex and vector beams based on Pancharatnam-Berry phase elements”, *Sci. Rep.* **7**, 44096 (2017).
- [33] N. A. Chaitanya, M. V. Jabir, and G. K. Samanta, “Efficient nonlinear generation of high power, higher order, ultrafast “perfect” vortices in green”, *Opt. Lett.* **41(7)**, 1348-1351 (2016).
- [34] M. V. Jabir, N. A. Chaitanya, A. Aadhi, and G. K. Samanta, “Generation of “perfect” vortex of variable size and its effect in angular spectrum of the down-converted photons”, *Sci. Rep.* **6**, 21877 (2016).
- [35] A. Banerji, R. P. Singh, D. Banerjee, and A. Bandyopadhyay, “Generating a perfect quantum optical vortex”, *Phys. Rev. A* **94**, 053838 (2016).
- [36] A. A. Kovalev, V. V. Kotlyar, and A. P. Porfirev, “A highly efficient element for generating elliptic perfect optical vortices”, *Appl. Phys. Lett.* **110**, 261102 (2017).
- [37] X. Li, H. Ma, C. Yin, J. Tang, H. Li, M. Tang, J. Wang, Y. Tai, X. Li, and Y. Wang, “Controllable mode transformation in perfect optical vortices”, *Opt. Express* **26(2)**, 651-662 (2018).
- [38] Y. Liang, M. Lei, S. Yan, M. Li, Y. Cai, Z. Wang, X. Yu, and B. Yao, “Rotating of low-refractive-index microparticles with a quasi-perfect optical vortex”, *Appl. Opt.* **57(1)**, 79-84 (2018).
- [39] Y. Liang, S. Yan, M. He, M. Li, Y. Cai, Z. Wang, M. Lei, and B. Yao, “Generation of a double-ring perfect optical vortex by the Fourier transform of azimuthally polarized Bessel beams”, *Opt. Lett.* **44(6)**, 1504-1507 (2019).
- [40] J. Yu, J. Wu, C. Xiang, H. Cao, L. Zhu, and C. Zhou, “A Generalized Circular Dammann Grating With Controllable Impulse Ring Profile”, *IEEE photon. Tech. Lett.* **30**, 801-804 (2018).

- [41] C. Zhou, J. Jia, and L. Liu, "Circular Dammann grating", *Opt. Lett.* **28(22)**, 2174-2176 (2003).
- [42] S. Zhao and P. S. Chung, "Design of a circular Dammann grating", *Opt. Lett.* **31(16)**, 2387-2389 (2006).
- [43] C. Zhou and L. Liu, "Numerical study of Dammann array illuminators," *Appl. Opt.* **34**, 5961-5969 (1995).
- [44] K. Rong, F. Gan, K. Shi, S. Chu, J. Chen, "Configurable Integration of On - Chip Quantum Dot Lasers and Subwavelength Plasmonic Waveguides", *Adv. Mater.* **30**, 1706546 (2018).
- [45] P. Vaity and L. Rusch, "Perfect vortex beam: Fourier transformation of a Bessel beam", *Opt. Lett.* **40**, 597-600 (2015).
- [46] V. Arrizón, U. Ruiz, D. Sánchez-de-la-Llave, G. Mellado-Villaseñor, and A. S. Ostrovsky, "Optimum generation of annular vortices using phase diffractive optical elements," *Opt. Lett.* **40**, 1173-1176 (2015).

## Supporting Information

### A generalized perfect vortex beam with controllable impulse ring profile

*Junjie Yu<sup>1+</sup>, Chaofeng Miao<sup>1,2,3</sup>, Jun Wu<sup>4</sup>, and Changhe Zhou<sup>1\*</sup>*

Corresponding Authors: E-mail: [+junjiey@siom.ac.cn](mailto:junjiey@siom.ac.cn) or [\\*chazhou@mail.shcnc.ac.cn](mailto:chazhou@mail.shcnc.ac.cn)

<sup>1</sup>Lab of Information Optics and Opto-electronic Technology, Shanghai Institute of Optics and Fine Mechanics, Chinese Academy of Sciences, P. O. Box 800-211, Shanghai 201800, China

<sup>2</sup>School of Physical Science and Technology, ShanghaiTech University, Shanghai 201210, China

<sup>3</sup>University of Chinese Academy of Sciences, Beijing 100049, China

<sup>4</sup>Department of Physics, Zhejiang University of Science and Technology, Hangzhou, 310023, China

#### Note S1: Theory of the Hankel transforming for circular gratings

It is known that the transmission function of a circular grating with radial periodic property can be decomposed into a series of circular cosine or sine functions with different frequencies [1].

And, the 2D Fourier transform (or called the zeroth Hankel transform) of the circular cosine/sine functions can be written as,

$$\cos(\alpha r) \stackrel{\text{H}}{\leftrightarrow} \frac{\alpha}{2} \frac{1}{(\alpha/2 + \pi\rho)^{3/2}} \delta^{(1/2)}(\alpha/2\pi - \rho), \quad (\text{s1-1a})$$

$$\sin(\alpha r) \stackrel{\text{H}}{\leftrightarrow} \frac{\alpha}{2} \frac{1}{(\alpha/2 + \pi\rho)^{3/2}} \delta^{(1/2)}(\rho - \alpha/2\pi), \quad (\text{s1-1b})$$

where  $\alpha$  is the scale parameter that determines the size of the impulse ring;  $\rho$  is the radial coordinate in the Fourier transforming plane, and  $\delta^{1/2}(\cdot)$  denotes the Dirac delta function. These two equations reveals well the impulse behavior of the Fourier spectrum of the circular sine and cosine functions. Of which, the two impulse rings  $\delta^{1/2}(\alpha/2\pi - \rho)$  and  $\delta^{1/2}(\rho - \alpha/2\pi)$  represent an inwards-oriented impulse ring and another outwards-oriented one, respectively. When a phase

shift  $\Delta\phi$  is introduced, a more generalized form of a circular cosine or sine function can be expressed as,

$$\cos(\alpha r + \frac{\Delta\phi}{2}) = u \cos(\alpha r) + v \sin(\alpha r), \quad (s1-2a)$$

$$\sin(\alpha r + \frac{\Delta\phi}{2}) = -v \cos(\alpha r) + u \sin(\alpha r), \quad (s1-2b)$$

where two weight coefficients are  $u = \cos(\Delta\phi/2)$ , and  $v = -\sin(\Delta\phi/2)$ . It means that the phase-shifted circular sine or cosine function can be expressed by a weight sum of two circular cosine and sine functions. For concision, we just discuss the case of circular cosine functions in the following. According to Eqs. (s1-1) and (s1-2), the Fourier transform of a phase-shifted circular cosine function can be written as,

$$H\{\cos(\alpha r + \Delta\phi/2)\} = \frac{\alpha}{2} \frac{1}{(\alpha/2 + \pi\rho)^{3/2}} \{u\delta^{1/2}(\rho - \alpha/2\pi) + v\delta^{1/2}(\alpha/2\pi - \rho)\}, \quad (s1-3)$$

where  $H\{\cdot\}$  denotes the zeroth order Hankel transformation. It is seen from this equation that the Fourier spectrum of a phase-shifted circular cosine function essentially denotes a weight sum of the spectra of circular cosine and sine functions. In further, when another spiral phase with topological charge of  $l$  is introduced, the Hankel spectrum of a circular cosine function can be derived as,

$$\begin{aligned} H\left\{\cos(\alpha r + \frac{\Delta\phi}{2})\exp(il\theta)\right\} &= 2\pi \exp(il\varphi) \int_0^\infty [u \cos(\alpha r) + v \sin(\alpha r)] J_l(2\pi\rho r) r dr, \\ &= 2\pi \exp(il\varphi)(uH_c + vH_s) \end{aligned} \quad (s1-4)$$

where the integrals  $H_c$  and  $H_s$  can be written as the  $l$ th order Hankel transform of circular cosine and sine functions, respectively, and these two integrals can be written in the form of piecewise functions as [2],

$$H_c = \int_0^\infty \cos(\alpha r) J_l(2\pi\rho r) r dr$$

$$= \begin{cases} \frac{(\rho/2\pi)^l \Gamma(l+2) \cos[\pi(l+2)/2]}{2^l \alpha^{(l+2)} \Gamma(l+1)} {}_2F_1(1+l/2, 3/2+l/2; l+1; (\rho/2\pi\alpha)^2), & 0 < \rho < 2\pi\alpha \\ \frac{2^{l-1} \Gamma(l/2+1)}{\Gamma(l/2)} {}_2F_1(1+l/2, 1-l/2; 1/2; (2\pi\alpha/\rho)^2), & \rho > 2\pi\alpha \end{cases}, \quad (\text{s1-5a})$$

$$H_s = \int_0^\infty \sin(\alpha r) J_l(2\pi\rho r) r dr$$

$$= \begin{cases} \frac{(\rho/2\pi)^l \Gamma(l+2) \sin[\pi(l+2)/2]}{2^l \alpha^{(l+2)} \Gamma(l+1)} {}_2F_1(3/2+l/2, 1+l/2; l+1; (\rho/2\pi\alpha)^2), & 0 < \rho < 2\pi\alpha \\ \frac{2^l \alpha \Gamma(l/2+3/2)}{(\rho/2\pi)^{l+1} \Gamma(l/2-1/2)} {}_2F_1(3/2+l/2, 3/2-l/2; 3/2; (2\pi\alpha/\rho)^2), & \rho > 2\pi\alpha \end{cases}, \quad (\text{s1-5b})$$

where  $\Gamma(\cdot)$  denotes a gamma function and  ${}_2F_1(a, b; c; x)$  is a hyper-geometric function. It indicates that there is a singularity at the position of  $\rho=2\pi\alpha$  for these two piecewise functions. It has been shown that these two piecewise functions essentially represent a pair of impulse rings, of which, one impulse rings with a trailing wake inward and the other one with a trailing wake outward [1]. Therefore, Fourier spectrum of the circular cosine function embedded with a spiral phase depicted in Eq. (s1-4) is can be seen as a weight sum of two impulse rings with coefficients of  $u=\cos(\Delta\phi/2)$ , and  $v=-\sin(\Delta\phi/2)$ , which are only determined by the phase delay  $\Delta\phi$ . It is suggest that an impulse ring vortex, i.e. a perfect optical vortex, could be generated and one can adjust the weights of those two impulse rings by changing the phase delay, and finally control arbitrarily the intensity profile of the impulse ring of the perfect vortex. It should be noted that the impulse ring would become a dark ring surrounded by two bright impulse rings in each side due to destructive interference of those inwards- and outwards-oriented impulse rings when those two coefficients have equal amplitude but opposite sign, i.e.  $u_m = -v_m$ .

### Note S2: Phase retrieval from six-step phase-shifted interferograms

In the experiment, the  $p$ -component is transmitted from the polarized beam splitter PBS1 and it is modulated by the SLM. Then, the modulated beam is reflected back and combined with the  $s$ -polarized part by another polarized beam splitter PBS2. The two parts with crossed

polarization are converted into a pair of circular polarized beams with inversed chirality after passing through a quarter wave-plate. Then, the interferogram after passing through the polarizer P2 can be written as,

$$I(x, y) = \frac{A_x^2}{2} + \frac{A_y^2}{2} + A_x A_y \cos[\phi(x, y) + 2\theta], \quad (\text{s2-1})$$

where  $A_x$  and  $A_y$  are the amplitudes of the two crossed polarized parts, and  $\phi(x, y)$  is the phase difference between them.  $\theta$  is the oriental angle of the polarizer P2. By rotating the oriental angle of the polarizer P2 with a step of  $\Delta\theta = \pi/6$  rad, we can obtain six phase-shifted interferograms. Then, the phase  $\phi(x, y)$  can be retrieved by [3],

$$\phi(x, y) = \begin{cases} \arctan(y/x) - \pi, & x > 0 \text{ and } y > 0 \\ \arctan(y/x), & x > 0 \text{ and } y < 0 \\ \arctan(y/x) + \pi/2, & x < 0 \end{cases}, \quad (\text{s2-2})$$

where,

$$\begin{aligned} X &= I_0 - 4I_2 + 3I_4 \\ Y &= -(3I_1 - 4I_3 + I_5) \end{aligned}, \quad (\text{s2-3})$$

and,

$$I_n = \frac{A_x^2}{2} + \frac{A_y^2}{2} + A_x A_y \cos[\phi(x, y) + 2n\Delta\theta], \quad n = 0, 1, 2, \dots, 5, \quad (\text{s2-4})$$

where  $\Delta\theta = \pi/6$  rad is the rotating step of the polarizer P2. Then, the phase carried by the POVs could be identified by the phase difference  $\phi(x, y)$  if only the reference beam is well-collimated and it can be seen as a plane wave. It should be pointed out that the phase difference also involve another part, i.e., the random phase disturbance caused by mechanical vibrations, air disturbances, temperature fluctuations, and also instability of the laser source. Here, we recorded a series of interferograms by the COMS camera (with frames rate 50 fps, and each video includes more than 1200 frames) instead by a single images for each step. For each video, those frames with contrast over than a threshold are chosen as the effective images waiting for

further processing. First, each effective frames is binarized. Next, those binarized images are summed up and the summation is binarized again. Then, calculating the correlation coefficients between each binarized frame and the above binarized summation and choosing the frame with the highest correlation coefficient as the interferogram for each step. Figure S1 shows a typical example of these six interferograms and also the corresponding retrieved phase for a dark POV with topological charge of  $l=-5$ .

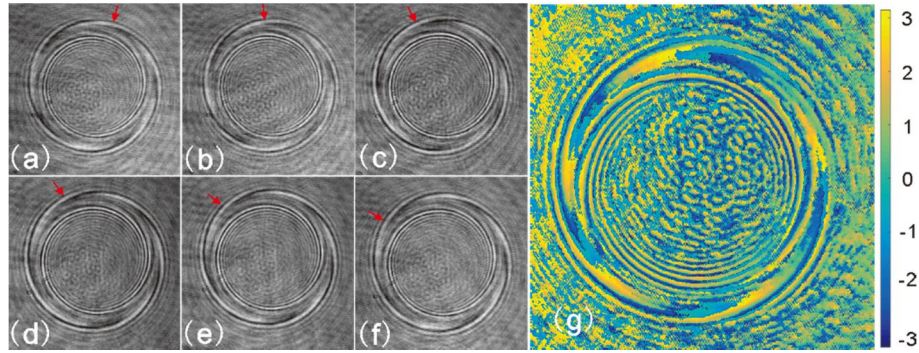


**Figure S1.** Illustration of an example of those six phase-shifted interferograms and the corresponding extracted phases at the defocused plane before the focus with phase step of  $\pi/3$  between any two adjacent images. (a)-(f) are interferograms with phase delay from 0 to  $5\pi/3$ , which is introduced by rotating the quarter waveplate with a step of  $\pi/6$  rad. (f) is the retrieved phase from those six interferograms.

## References

- [1] I. Amidror, *J. Opt. Soc. Am. A* **14**, 816-826 (1997).
- [2] H. Bateman, McGraw-Hill Book Company, New York (1954).
- [3] Yves Surrel, "Design of algorithms for phase measurements by the use of phase stepping," *Appl. Opt.* **35**, 51-60 (1996).